

Article

Revealing the Relationship Between Macrostructures and Inclusions Across the Thickness Direction of Q235B Slabs

Bo Wang ¹, Jinwen Jin ², Chao Gu ^{1,*} , Ze Wei ², Ziyu Lyu ¹, Lidong Xing ^{1,3} and Yanping Bao ^{1,*}

¹ State Key Laboratory of Advanced Metallurgy, University of Science and Technology Beijing, Beijing 100083, China; wb08080419@163.com (B.W.); lvziyu163@163.com (Z.L.); xinglidong@ustb.edu.cn (L.X.)

² Ningbo Iron and Steel Co., Ltd., Ningbo 315807, China; lkx04190808@163.com (J.J.); lihaozhe112@163.com (Z.W.)

³ Technical Support Center for Prevention and Control of Disastrous Accidents in Metal Smelting, University of Science and Technology Beijing (USTB), Beijing 100083, China

* Correspondence: guchao@ustb.edu.cn (C.G.); baoy@ustb.edu.cn (Y.B.)

Abstract: Macrostructures and inclusions are both vital for slabs because the quality of slabs is largely affected by them. However, the relationship between macrostructures and inclusions in the thickness direction of the slab is still unclear. Hence, in this paper, the relationship between macrostructures and inclusions was revealed by laboratory experiments and theoretical calculations. The laboratory experiments included carbon and sulfur content testing, direct reading spectroscopy, scanning electron microscopy, and automatic inclusion scanning. The experimental results showed that the distribution of macrostructures was symmetrical from the inner and outer arc to the center. From the edge to the center of the slab, the variation in macrostructures was columnar crystal zone (CZ)→columnar-to-equiaxed transition (CET)→equiaxed crystal zone (EZ). Furthermore, the content of sulfur and manganese first decreased and then increased from the inner arc to the outer arc. The number density and area fraction of MnS inclusions in different macrostructures were CZ > CET > EZ. The average size of MnS in different macrostructures was CZ > EZ > CET. Moreover, the morphology of MnS inclusions was ellipse and rod in CZ, irregular dendrite in CET, and multilateral in EZ. Additionally, theoretical calculation results showed the maximum precipitation and initial precipitation temperature of MnS inclusions in different macrostructures were CZ > EZ > CET. Meanwhile, the theoretical precipitation radius of MnS inclusions in different macrostructures was CZ > EZ > CET.

Keywords: Q235B steel; macrostructures; dendrite; inclusions; slab; thermodynamics; kinetics



Citation: Wang, B.; Jin, J.; Gu, C.; Wei, Z.; Lyu, Z.; Xing, L.; Bao, Y. Revealing the Relationship Between Macrostructures and Inclusions Across the Thickness Direction of Q235B Slabs. *Crystals* **2024**, *14*, 1010. <https://doi.org/10.3390/cryst14121010>

Academic Editor: José L. García

Received: 9 November 2024

Revised: 17 November 2024

Accepted: 18 November 2024

Published: 21 November 2024



Copyright: © 2024 by the authors. Licensee MDPI, Basel, Switzerland. This article is an open access article distributed under the terms and conditions of the Creative Commons Attribution (CC BY) license (<https://creativecommons.org/licenses/by/4.0/>).

1. Introduction

During the metallurgical production process, the properties of the final products are largely affected by the quality of the slab. Meanwhile, the macrostructure and inclusions in the slab are two key factors that affect its quality [1–6].

On the one hand, the macrostructure in slabs mainly includes columnar crystal, equiaxed crystal, and so on. The macrostructure determines the mechanical processing properties and service life of the slab [5,7–9]. Excellent macrostructure can provide uniform structure and stable performance, while a poor macrostructure may lead to cracks, deformation, and other problems in the slab [10–13]. Recently, a lot of research has been conducted on the distribution of macrostructure in the thickness direction of the slab. Choudhary et al. [14] found that columnar crystals accounted for a large proportion of the macrostructures in the slabs, which is detrimental to internal soundness. The research of Ganguly et al. [15] revealed that a fully equiaxed structure was observed in the center of the slab and a mixed columnar-equiaxed region was observed in 6–10 mm from the center at the same time. Li et al. studied the solidification behavior in the thickness of grain-oriented silicon steel continuous casting slab and found that the center of the slab was the equiaxial crystal zone, and the edges were the columnar crystal zone.

On the other hand, inclusions are unavoidable in the slab. The main types of inclusions in the slab are TiN and MnS [16–19]. Furthermore, the type, quantity, size, morphology, and distribution of inclusions have a significant impact on the quality of the slab [20–23]. Substantial studies have been conducted on the distribution of inclusions across the thickness direction of the slab. Deng et al. [24] found that Al₂O₃ was the main inclusion in a low-carbon aluminum-killed steel slab and mainly concentrated within the zone 3.5–6 mm from the inner arc of the slab. The research of Yu et al. [25] revealed that MnS inclusions have the largest average diameter of 6.35 μm and an area fraction of 2.5×10^{-4} across the medium carbon structural steel slab thickness. MnS inclusions will affect the machinability and mechanical properties of steel. Ghosh et al. [26] found that MnS inclusions with long and thin thickness were the main cause of pressure ductility and impact toughness anisotropy of rolled plates. By using the finite element method combined with a laboratory high-temperature tensile test, Wang et al. [27] found that there is a large difference in strength and toughness between steel with and without MnS inclusions at 900–1200 °C. Researchers have also conducted a lot of research on the reasons why MnS affects the properties of steel. Wu et al. [28] found that the smaller the area fraction of MnS inclusions, the smaller the area of zonal cracks with the most local deformation. Yamamoto et al. [29] found that fine-grained MnS inclusions could easily cause cracks. Chu et al. [30] found that the more dispersed the MnS inclusions were, the better the formability of medium- and high-manganese steel was. It can be seen from the above that the influence of MnS inclusions on the mechanical properties of steel is mainly related to their morphology, size, and distribution, so it is necessary to discuss the precipitation rule of MnS inclusions in Q235B steel in detail.

Q235B carbon structural steel is widely used because of its brilliant toughness, strength, and weldability. At present, it is mainly used in steel plates, steel bars, bridge construction, and other fields because the production of this steel is cost-effective, and it is easy to manufacture [31–33]. It can be seen from the above that scholars have carried out substantial research on the macrostructure and inclusions of slabs. However, the relationship between macrostructure and inclusion precipitation in the thickness of the Q235B steel slab remains unclear. Therefore, in order to control the formation of inclusions and improve macrostructure, it is necessary to deeply study the relationship between the macroscopic structure and inclusions in the slab.

Based on this, the relationship between macrostructure and the type, number density, size, and morphology of inclusions in the Q235B steel slab is studied in this paper by experimental research and theoretical calculation. This study provides a scientific basis for optimizing the casting process, controlling the formation of inclusions, and improving the macrostructure of the slab, so as to improve the quality of the slab to meet the increasingly strict industrial requirements.

2. Materials and Methods

The experimental material of this paper was taken from the carbon structural steel Q235B produced by a steel plant. The smelting process of this steel is as follows: “converter→Ar station→LF refining→50 tons large capacity T-tundish→slab continuous casting machine”. After the hot metal was poured into the converter, the coke, limestone, dolomite, and magnesite were added into the converter. Subsequently, the ferromanganese, manganese, and Al wires were added into the molten steel in an Ar station. The specific process flow chart is shown in Figure 1.

The composition control requirements of the Q235B steel are shown in Table 1.

Table 1. Chemical composition control requirements for Q235B (wt%).

Element	C	Si	Mn	P	S	Alt	Fe
Content	0.075	0.18	0.38	≤0.020	0.015	0.010	Bal.

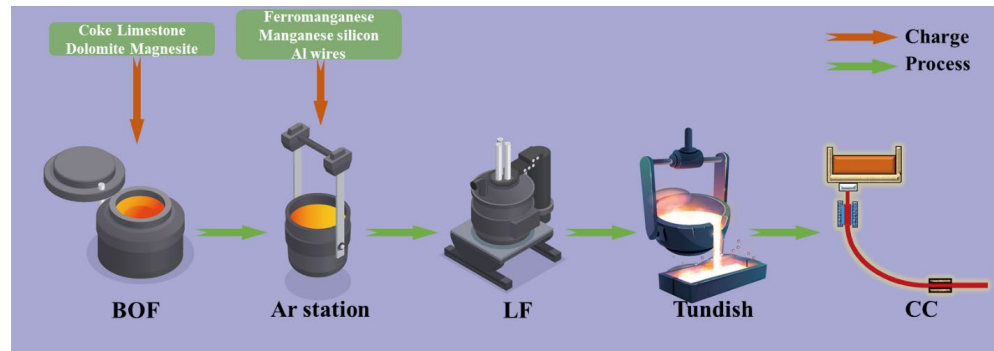


Figure 1. Production process of Q235B.

The slab of one treatment of Q235B smelting was sampled and analyzed, and the specific sampling scheme and research method are shown in Figure 2. Twelve $10 \times 10 \times 10 \text{ mm}^3$ metallographic samples were taken from the inner arc to the outer arc of the slab, numbered C1–C12. The weight of each metallographic sample was about 6.5 g. Metallographic samples were processed by a thermal automatic insert machine (OPAL-410) and an automatic grinding and polishing machine (SAPHIR-550). After embedding, grinding, and polishing, the metallographic samples were affixed with aluminum foil and conductive adhesive on the tested surface and were sent to the automatic inclusion scanning analyzer (ZEISS). Subsequently, metallographic samples were scanned for inclusions by ASPEX (automatic inclusion scanning microscopy) with AFA technology to analyze the variation in inclusion type, quantity, and size, with a scanning area of $2.96 \times 10^7 \mu\text{m}^2$. Then, 3 mm of scraps was drilled on the surface of the metallographic sample, and the change in carbon and sulfur content in the thickness direction of the slab was analyzed by a carbon and sulfur analyzer (EMIA-920V2). The morphology, type, and size of inclusions were characterized by scanning electron microscopy (MLA-250). A total of 12 $\Phi 15 \times 5 \text{ mm}$ cylinder samples were taken from the inner arc to the outer arc of the slab, and the change in Mn content in the thickness direction of the slab was detected by the direct reading spectrum (ARL-8860). Finally, the surface of the sample C1–C12 was etched with hydrochloric acid, and its macrostructure was observed.

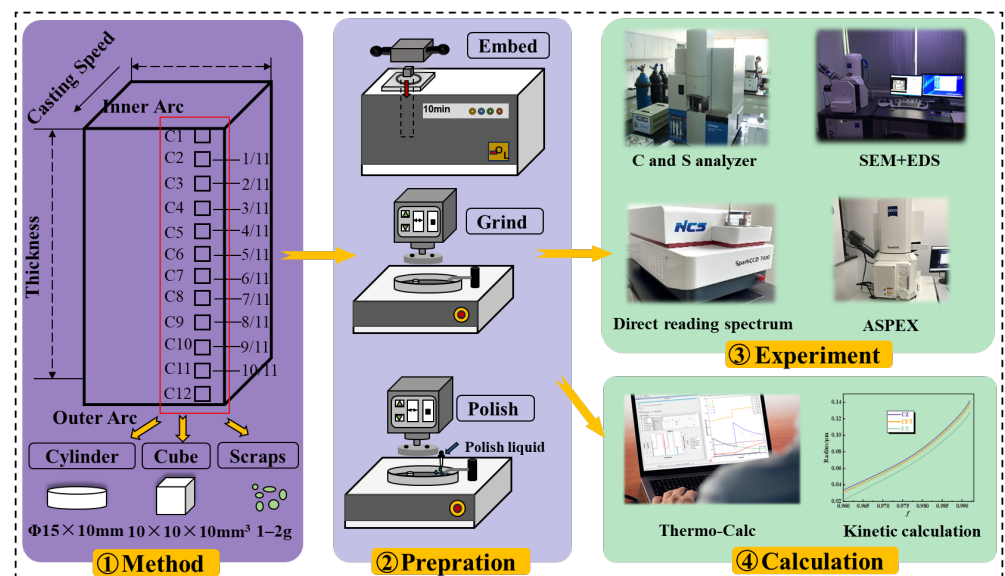


Figure 2. Sampling scheme and research method.

3. Results and Discussion

3.1. Variation in the Macrostructure in the Thickness Direction of Slab

Figure 3 illustrates the variation in the macrostructure in the thickness direction of the slab. It can be seen that from the inner arc to the center of the slab, the macrostructure changes from the columnar crystal zone (referred to as CZ in the following) to the columnar crystal to equiaxial crystal transition zone (referred to as CET in the following). At the center of the slab, the macrostructure changes to an equiaxial crystal zone (referred to as EZ in the following). It is worth mentioning that from the outer arc to the center, the variation in the macrostructure is also the same. Therefore, it can be concluded that the macrostructure distribution in the thickness direction of the slab is symmetrical from the center to the inner arc and outer arc. Therefore, the variation in the macrostructure from the edge to the center is columnar crystal region (CZ)→columnar crystal to equiaxed crystal transition region (CET)→equiaxed crystal region (EZ), which is consistent with the conclusion of Yao et al. [34]. In addition, the possible reason for the formation of different macrostructural regions along the thickness direction of the slab may be different cooling rates at different locations. The inner and outer arcs of the slab usually have a higher cooling rate, which is conducive to the growth of columnar crystals. With the transition from the edge to the center, the cooling rate gradually decreases, which provides more favorable conditions for the growth of equiaxed crystals.

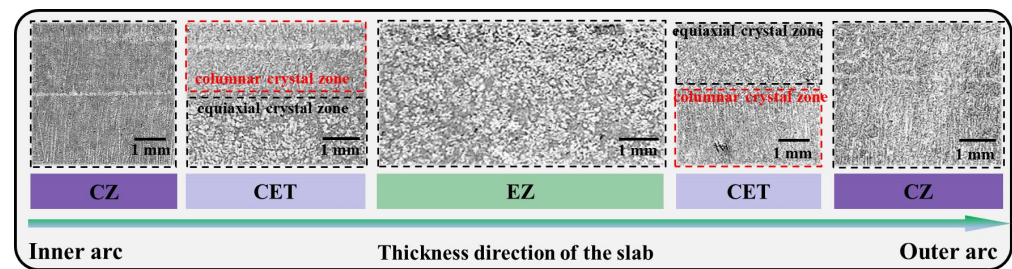


Figure 3. Variation in the macrostructure in the thickness direction of the slab.

Secondary dendrite spacing (SADS) is a comprehensive characterization of dendrite growth rate and cooling rate during solidification. According to the method of calculating SADS based on carbon content and cooling rate proposed by Won et al. [35] in the literature, the variation in SADS in the thickness direction of the Q235B slab was studied. The specific calculation method is shown as follows:

$$\lambda = (169.1 - 720.9 \cdot [\%C] \cdot v_c^{-0.4935}) \quad (1)$$

where [%C] represents the carbon content in the slab, which can be measured by the carbon sulfur analyzer (Figure 2). v_c represents the cooling rate, which is 10 K/s according to the on-site production condition. According to Equation (1), the variation in secondary dendrite spacing in the thickness direction of the slab can be obtained in Figure 4. It can be seen that SADS showed a gradually increasing trend from the inner and outer arc to the center of the slab. Purple stands for CZ, light purple for CET and green for EZ. The SADS of the equiaxed crystal region was larger than the columnar crystal region, which is consistent with the research result of Gu et al. [36]. The possible reason is that the SADS is smaller because of the large undercooling degree and high nucleation rate at the edge of the slab, so the secondary dendrite growth was limited. In the center of the slab, the secondary dendrites have more space to grow, and the SADS is larger. Large SADS tends to lead to the enrichment of solute elements and serious segregation. It is worth mentioning that the difference in SADS values in the thickness direction of the slab is small, which can effectively prevent the appearance of cracks in the slab.

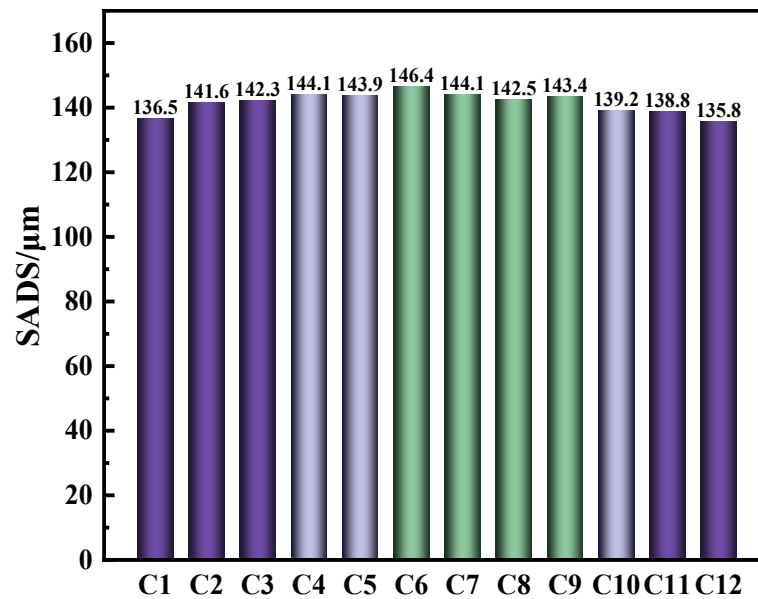


Figure 4. Variation in SADS in the thickness direction of the slab.

3.2. The Relationship Between Inclusion Precipitation and Macrostructure in the Thickness Direction of Slab

In order to investigate the law of inclusion precipitation in the solidification process of the slab, the law of inclusion precipitation was calculated by Thermo-Calc (2018) software. As shown in Figure 5, the main inclusion formed in the Q235B slab was MnS. MnS precipitated at 1393 °C, and the precipitation amount increased with the degradation of temperature. Finally, the precipitation amount remained stable at 1200 °C.

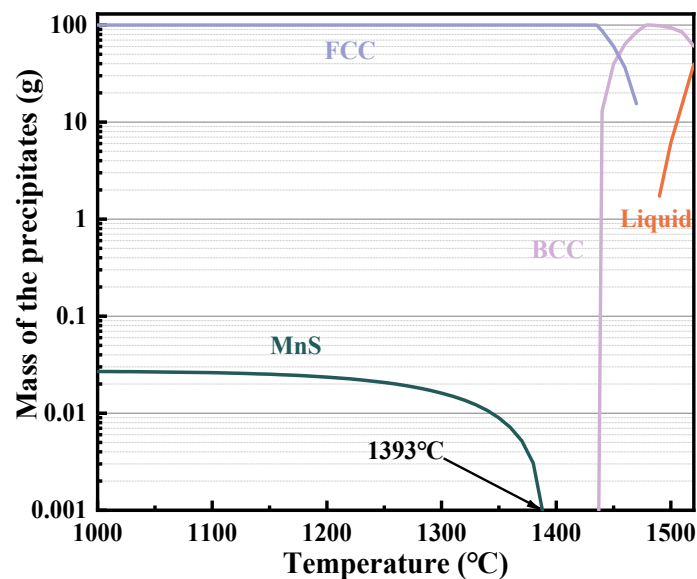


Figure 5. Relationship between inclusions and temperature at the equilibrium.

Figure 6 illustrates the variation in manganese and sulfur content in the thickness direction of the slab. The lowest manganese content was found in sample C6, which was about 0.39%. On the whole, the manganese content was the lowest in the center of the slab and higher in the inner and outer arc. The lowest sulfur content was 0.0228% (weight percent) in sample C7. The content of sulfur content was the highest in the center of the slab and gradually decreased in the direction of the inner and outer arc. It can be seen that

the content of manganese and sulfur was higher at the edge of the slab, where it is easy for them to segregate and MnS inclusions to form [37].

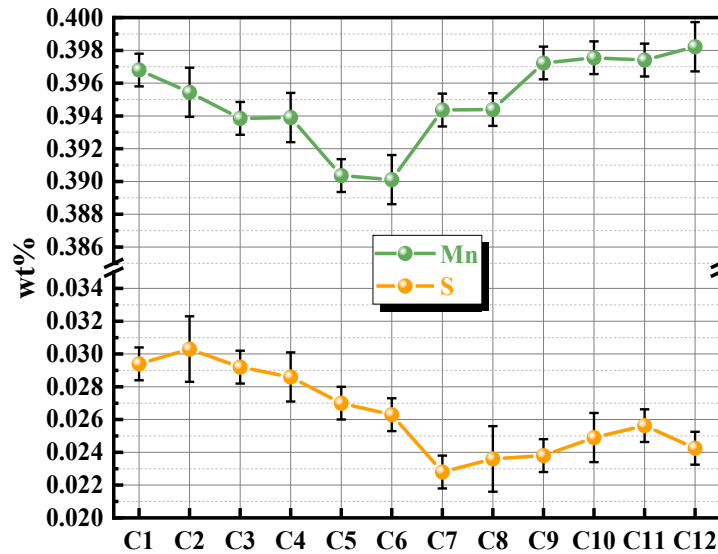


Figure 6. Variation in the content of manganese and sulfur in the thickness direction of the slab.

According to Figure 5, the main inclusion type in the slab is MnS. The automatic inclusion scanning method was used to collect the statistics on the characteristics of MnS inclusions. The variation in the area fraction of MnS inclusions in the slab thickness direction is shown in Figure 7. It can be seen from Figure 7 that the area fraction of MnS inclusions was larger at the edge and lower at the center of the slab. Therefore, the area fraction of MnS from the center to the edge of the slab is symmetrical. Furthermore, MnS inclusions are more distributed in the columnar crystal region and less in the equiaxed crystal region across the thickness direction of the slab. All in all, it can be concluded that the area fraction of MnS continuously decreased from CZ (6.198) → CET (3.52) → EZ (3.43) by averaging the data of the test samples in different macrostructures.

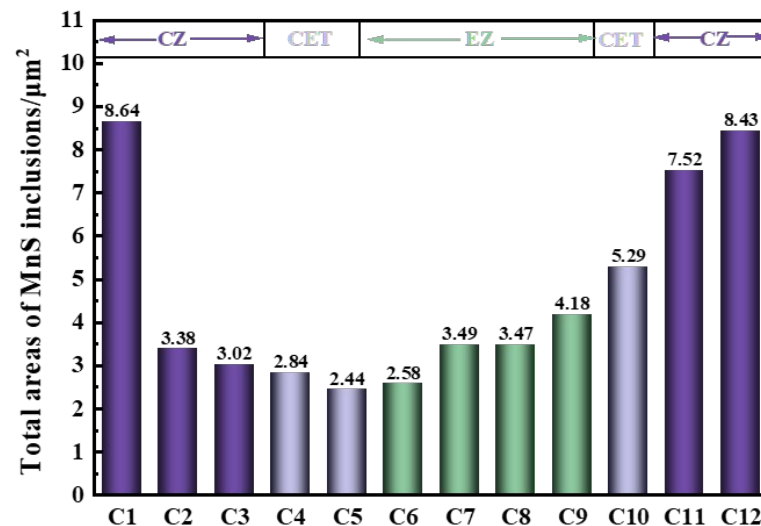


Figure 7. Variation in the total area of MnS inclusions in the thickness direction of the slab.

The number of MnS inclusions of different sizes is shown in Figure 8a. It can be seen that most of the dimensions of MnS inclusions were less than 5 μm in the thickness direction of the slab. Most of the dimensions are concentrated within the 1–2 μm range. Inclusion within the 1–2 μm range first decreased and then increased from the inner arc to

the outer arc in the thickness direction of the slab, which is the same as the total number of MnS. There are almost no inclusions larger than 10 μm in the thickness direction of the slab. The proportion of MnS inclusions of different sizes is shown in Figure 8b. The inclusions of 1–2 μm were more than 85% at 5/11 and 6/11 distance from the inner arc of the slab. In the center of the slab, the proportion of 3–5 μm inclusions was the largest, which is 32%. The inclusions with a size greater than 10 μm in the inner arc and outer arc of the slab were relatively large, which may be due to the serious segregation of manganese and sulfur at the edge of the slab. The large size of inclusions in the inner and outer arcs of the slab may also be due to the cooling rate of the slab edge being small so that the MnS inclusions have enough time to grow, which leads to the size of MnS inclusions being larger.

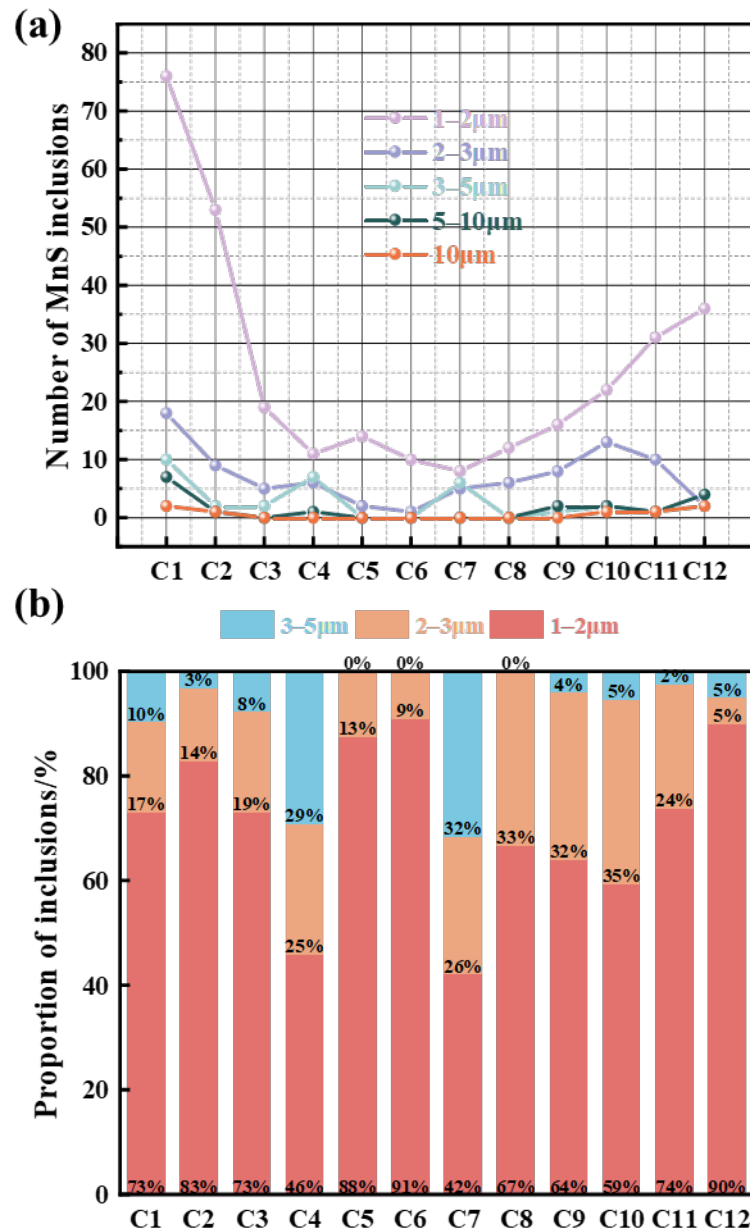


Figure 8. Number of different sizes (a) and proportion (b) of MnS inclusions in the thickness direction of the slab.

The variation in the average size of MnS inclusions in the thickness direction of the slab is shown in Figure 9a. In Figure 9a, purple stands for CZ, light purple for CET and green for EZ. It can be seen that the average size of MnS inclusions in the inner and outer

arc of the slab was higher than 2 μm . In other words, the average size of MnS inclusions in the columnar crystal region was smaller. This may be due to the lower cooling rate at the edge of the slab, so MnS inclusions have more time to grow. The average size of MnS inclusions in the equiaxed zone was smaller than the columnar zone but larger than the transition zone. Based on the research result of Wang et al. [31], the smaller size of MnS inclusions in the equiaxial region may be due to the precipitation time of MnS inclusions in the equiaxed zone being late, which limits the growth of inclusions. Therefore, the growth of inclusions in all directions is more balanced in the equiaxial region, and it is difficult to form larger inclusions. Variation in the distribution law of MnS inclusions of different sizes in the thickness direction of the slab is shown in Figure 9b. The pink boxes represent the middle 50% of the data. The bottom of the box is the lower quartile, the top is the upper quartile, and the line inside the box indicates the median. It can be seen that the maximum size of inclusions in the columnar crystal region was about 10 μm , and the inclusions in the equiaxial crystal region were concentrated within the 1–3 μm range. So, it can be concluded that the sizes of MnS inclusions were CZ (1.924) > EZ (1.7) > CET (1.495) by averaging the data of the test samples of different macrostructures.

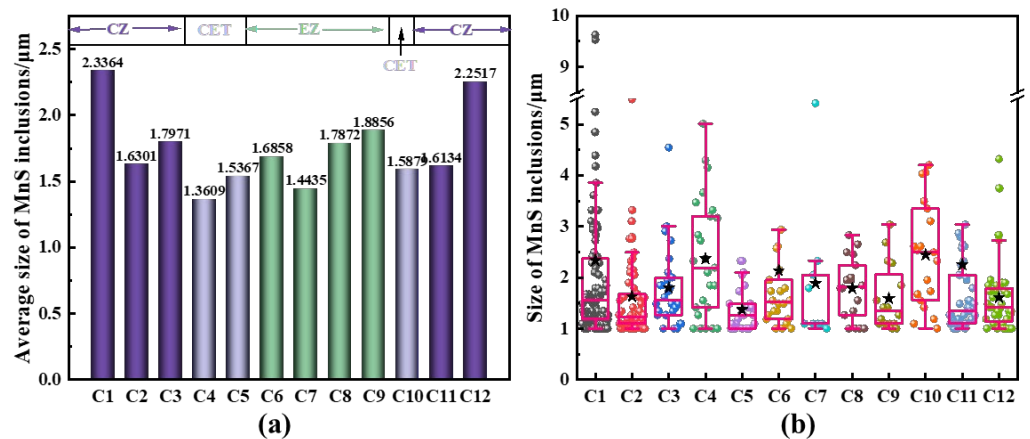


Figure 9. Average size (a) and size distribution (b) of MnS inclusions in the thickness direction of the slab.

It can be seen from Figure 4 that the secondary dendritic arm spacings showed a gradually increasing trend from the inner and outer arc to the center of the slab. According to Figures 7–9, it can be concluded that the amount and size of MnS inclusions in the region with large secondary dendritic arm spacings are lower. This may be due to the larger spacings between secondary dendrites, as solute elements in steel are not easily enriched, so fewer MnS inclusions are formed [28].

In order to study the distribution of inclusions in the thickness direction of the slab more comprehensively, the size and area fraction of inclusions are presented by the cloud map. The cloud map of MnS inclusion size and area fraction distribution in the thickness direction of the slab is shown in Figure 10. The color from purple to red indicates an increasing inclusion size and area fraction. It can be seen that the size and area fraction of inclusions were smaller in the center and larger at the edge of the slab, which is consistent with the results of Figures 6 and 7. There are more large inclusions in 2/11–3/11 from the outer arc, which may be due to the enrichment of manganese and sulfur, resulting in the easier formation of MnS inclusions.

In this study, cloud maps are used to more fully investigate the distribution of elements in the thickness direction of the slab. The content distribution of manganese and sulfur of inclusions with different sizes is shown in Figure 11. It can be seen that the mass fraction of manganese and sulfur of 1–2 μm inclusions in the center of the slab was higher, which was 40–50%. It may be due to the uneven secondary cooling strength in the continuous casting process, resulting in a small cooling rate in the center of the slab, which leads to manganese and sulfur gathering in the central area of the slab. The mass fraction of manganese in the

inclusions with size 2–3 μm in the inner arc of the slab was higher, but the mass fraction of sulfur was significantly lower than the inclusions with size 1–2 μm . The mass fraction of sulfur and manganese in the inclusions with size 3–5 μm was more evenly distributed, and the mass fraction of manganese was larger in the center of the slab.

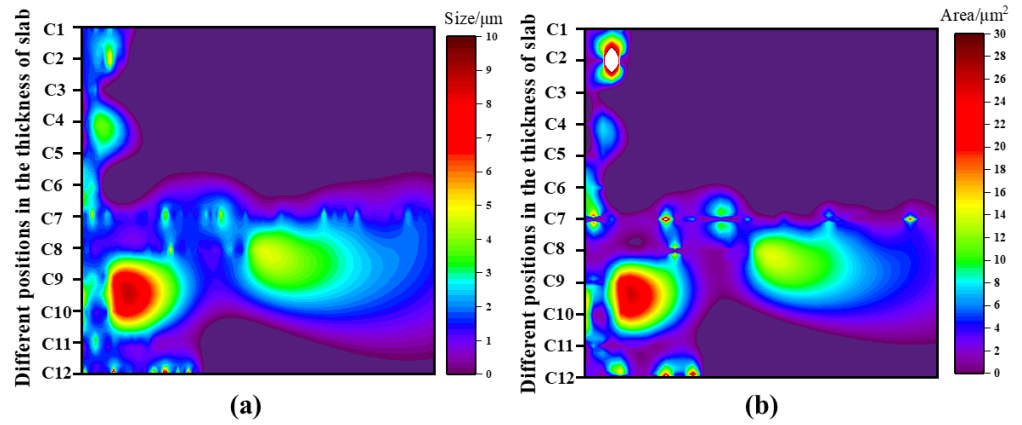


Figure 10. Size (a) and area fraction (b) distribution of MnS inclusions in the thickness direction of the slab.

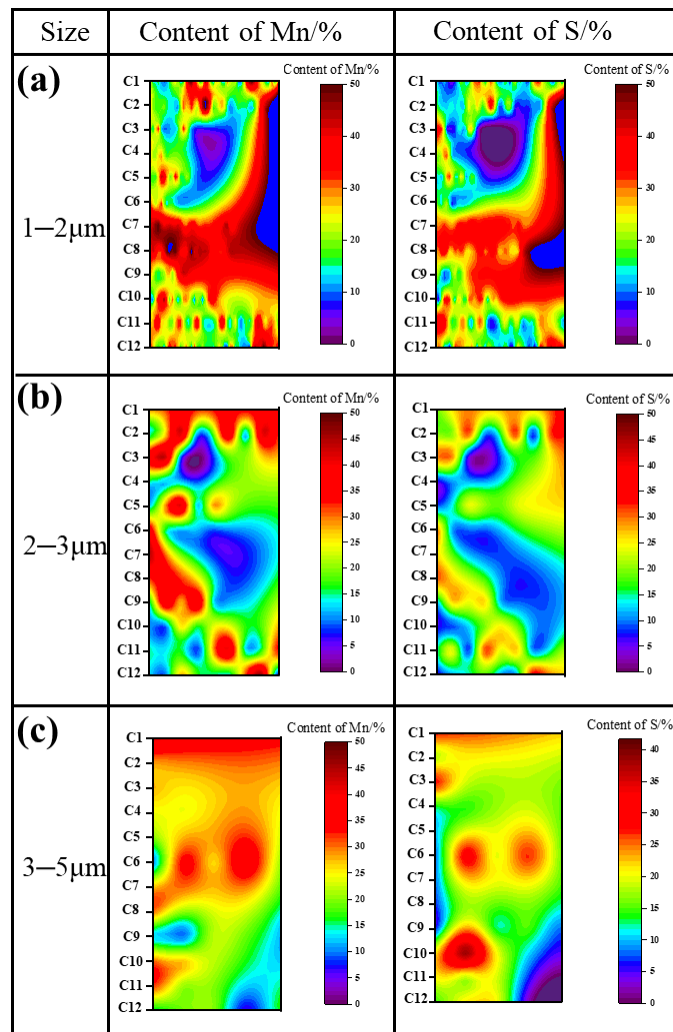


Figure 11. Content distribution of manganese and sulfur of 1–2 μm (a), 2–3 μm (b), and 3–5 μm (c) inclusions.

The morphology variation of inclusions in the thickness direction of the slab is shown in Figure 12. Red represents aluminum in this figure, purple represents oxygen, blue represents manganese and yellow represents sulfur. The stuff in the red box represents the inclusion. It can be seen that the morphology of MnS inclusions was mainly ellipse and rod in the columnar crystal region. In the transition zone, MnS inclusions exist in the slab in the form of irregular dendrites, and the size was larger. MnS inclusions mainly exist in the form of wrapping around the Al₂O₃ complex inclusions in the equiaxed crystal region, and the morphology was mainly quadrilateral and pentagonal. The reason why the morphology changed may be that the cooling rate, chemical composition distribution, and solidification process are different in the direction of the thickness of the slab. MnS inclusions mostly appear in the columnar zone and columnar-to-equiaxed transition zone, but the inclusion morphologies of the two zones are totally different. It may be caused by inconsistency in formation temperature and segregation.

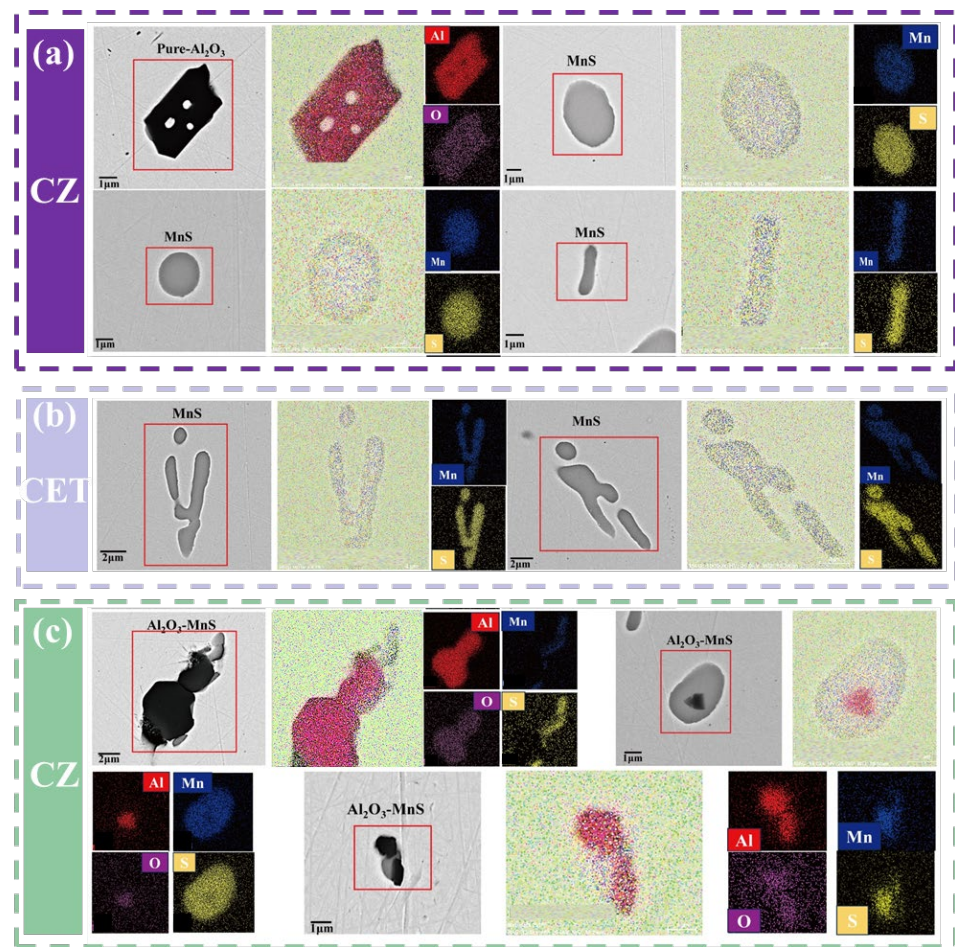


Figure 12. Variation in morphology at different macrostructures: CZ (a), CET (b), and CZ (c).

3.3. Thermodynamic Calculation

In order to further study the relationship between MnS inclusion precipitation and macrostructure in the thickness direction of the slab, the segregation of Mn and S in the slab was calculated by thermodynamics. With the solidification process of liquid steel, solute elements will be enriched in the liquid phase. Selective crystallization will occur at the solidification front, resulting in segregation and precipitation. According to the Scheil equation [30], the relationship between the content of solute elements at the solidification front and the solidification fraction f of liquid steel is as follows [38]:

$$C_L = C_0(1 - f)^{(k-1)} \quad (2)$$

where C_L represents the mass fraction of solute elements along the solidification front, C_0 denotes the initial mass fraction of solute elements in the liquid steel, f indicates the solidification ratio, and k represents the equilibrium distribution coefficient of solute elements. Moreover, with $k_{Mn} = 0.78$, $k_S = 0.035$ [27].

The segregation ratio of solute elements in the liquid phase during solidification is expressed as C_L/C_0 [28]. According to Equation (2), the relationship between the segregation ratio of Mn and S and the solidification coefficient f can be obtained in Figure 13. It can be seen that Mn and S have a large degree of segregation in the middle and late solidification. The degree of segregation of S is greater than Mn.

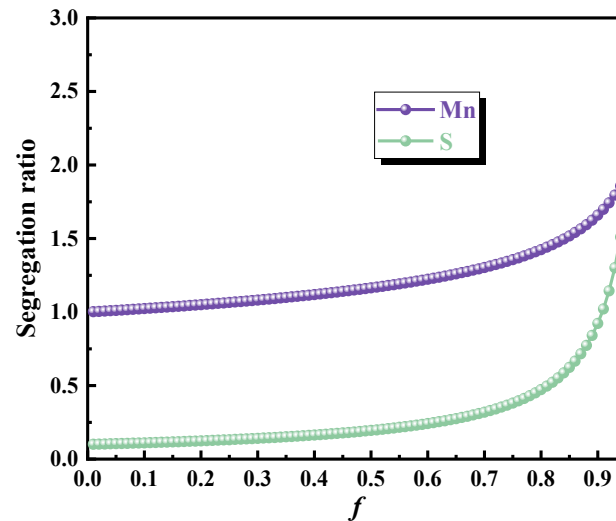


Figure 13. Tendency of different elemental segregation.

According to the above element detection results, it can be concluded that the content of Mn was 0.3963% (weight percent; the element content “%” in the subsequent text indicates this meaning) and the content of S was 0.0277% in CZ. The content of Mn was 0.3939%, and the content of S was 0.0268% in CET. Moreover, the content of Mn was 0.3902%, and the element content of S was 0.0241% in CZ. Thermodynamic software ThermoCalc (2018) was used to calculate the precipitation curves of inclusions in different macrostructures, as shown in Figure 14. The maximum precipitation of MnS inclusions in CZ was the largest, CET was the second, and EZ was the smallest. The results are consistent with those obtained in the above laboratory experiments. Moreover, the initial precipitation temperature of MnS in EZ was the lowest (1430 °C) during the solidification process, CET was the second (1445 °C), and CZ was the highest (1450 °C) (Figure 14d).

In order to study the precipitation law of MnS in solidification, the precipitation curves of MnS inclusions in different macrostructure regions were calculated by the thermodynamic method. The relationship between the actual concentration product Q_{MnS} , the theoretical concentration product K_{MnS} , and the solidification coefficient f was calculated by using our previous research method [38,39], as shown in Figure 15. It can be seen that when f was greater than 0.964 in CZ, $\lg Q_{MnS} > \lg K_{MnS}$, the actual concentration product of MnS at the solidification front was greater than the theoretical concentration product, and MnS could be precipitated. The critical f of MnS precipitation for CET and EZ was, respectively, 0.976 and 0.983, which is consistent with the thermodynamic calculation above. It can be seen from Figure 15d that the critical f of MnS precipitation was: CZ (0.964) < EZ (0.976) < CET (0.983).

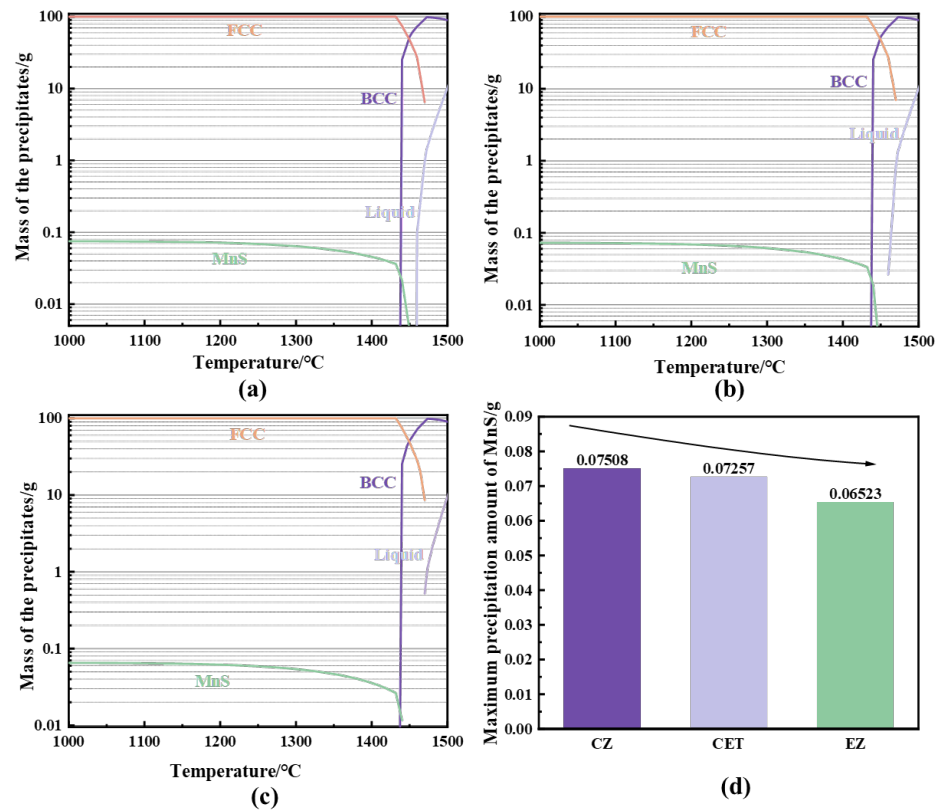


Figure 14. Precipitation curves of MnS in CZ (a), CET (b), and EZ (c) and maximum precipitation of MnS in different macrostructures (d).

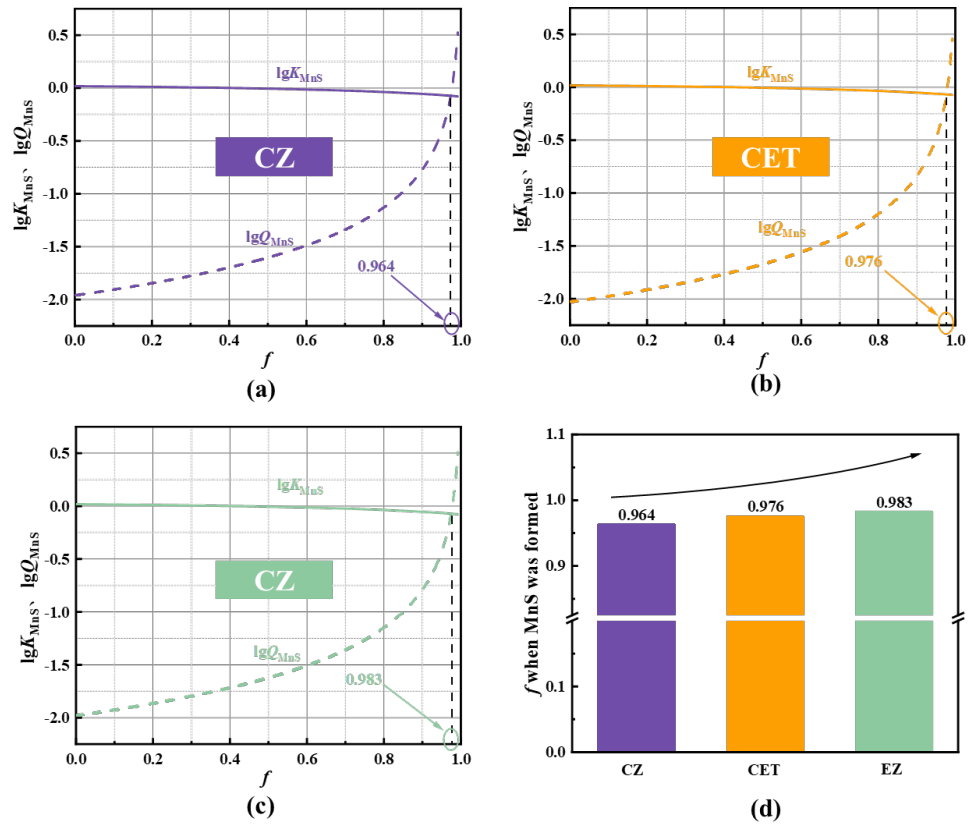


Figure 15. Precipitation curves in CZ (a), CET (b), and EZ (c) and solidification coefficient f in different macrostructures.

3.4. Kinetic Calculation

In this paper, the liquid-phase line temperature (T_L) and solid-phase line temperature (T_S) of Q235B steels were calculated by using the following equations:

$$T_S = 1809 - 184.3[\%C] - 40.8[\%Si] - 8.6[\%Mn] - 3.4[\%Cr] - 76.7[\%P] - 76.7[\%S] - 7.8[\%Al] \quad (3)$$

$$T_L = 1809 - 78[\%C] - 7.6[\%Si] - 4.9[\%Mn] - 1.3[\%Cr] - 34.4[\%P] - 38[\%S] - 3.6[\%Al] \quad (4)$$

Based on Equations (2) and (3) and the chemical composition of the Q235B steel, $T_L = 1806$ K and $T_S = 1795$ K were calculated.

The theoretical precipitation size r of MnS inclusions can be expressed as

$$r \frac{dr}{dt} = \frac{M_s}{100M_m} \cdot \frac{\rho_m}{\rho_s} D_i ([\%i]_L - [\%i]_e) \quad (5)$$

Integrating Equation (5),

$$r = \sqrt{\frac{M_s}{50M_m} \cdot \frac{\rho_m}{\rho_s} D_i ([\%i]_L - [\%i]_e) \cdot (1-f) \cdot \tau} \quad (6)$$

$$\tau = \frac{T_L - T_S}{v_c} \quad (7)$$

Please refer to our previous research for the expression of each physical quantity in the formula [38]. Equation (6) was substituted into Equation (5) to calculate the relationship between the precipitation size of MnS and the solidification coefficient f . As shown in Figure 16, the theoretical MnS precipitation radius of CZ was the largest, CET was the second, and EZ was the smallest. Probably because the CZ zone cooled and solidified later, MnS had more time to grow and aggregate, so the size was larger. Meanwhile, the results of the above laboratory tests showed that the content of Mn and S was higher at the edge of the slab, which makes it easier for them to segregate and promote the growth of MnS inclusions.

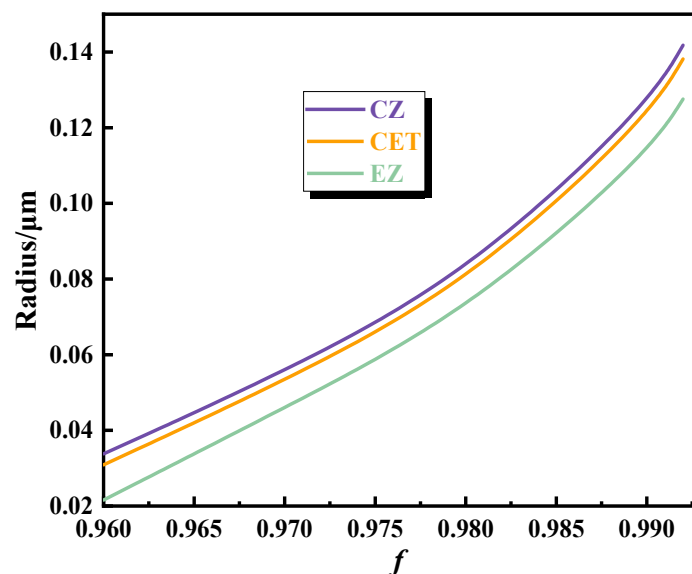


Figure 16. Precipitation radius of MnS inclusions in different macrostructures.

As for the variation of inclusions in the thickness direction of the Q235B steel slab, the theoretical calculation results are consistent with the experimental results on the whole, but there are some differences. The differences may be caused by different cooling rates in the thickness direction of the slab, uneven distribution of chemical components, different

solidification paths, dendrite growth, and experimental instrument error. This study aimed to reveal the relationship between the macrostructures and inclusions in the thickness direction of the slab, so there may be some limitations in the error between the predicted value and the measured value. If we further study this topic, we will focus on more accurate thermodynamic and kinetic models to predict the distribution of inclusions in the Q235B slab.

4. Conclusions

In this paper, the relationship between the macrostructure and inclusions in the thickness direction of the slab was elucidated, and the following conclusions were obtained:

- (1) The transformation in the macrostructure from the inner and outer arc to the center was symmetry: columnar crystal region (CZ)→columnar crystal to equiaxed crystal transition region (CET)→equiaxed crystal region (EZ). The difference in SADS values in the thickness direction of the slab was small, and the SADS of EZ was larger than CZ.
- (2) The content of Mn and S was first increased and then decreased from the inner arc to the outer arc in the thickness of the slab.
- (3) Thermodynamics calculation results showed that the maximum precipitation of MnS inclusions at different macrostructures was CZ > EZ > CET. The initial precipitation temperature of MnS inclusions in CZ was the largest (1450 °C), CET was the second (1445 °C), and EZ was the smallest (1430 °C).
- (4) In different macrostructures, the area fraction of MnS inclusions was CZ (6.198) > CET (3.52) > EZ (3.43), and the sizes of MnS inclusions were CZ (1.924) > EZ (1.7) > CET (1.495). Kinetic calculation showed that the theoretical precipitation radius of MnS inclusions with different macrostructures was CZ > CET > EZ. The morphology of MnS inclusions was elliptical and rod-like in CZ, irregular dendrite in CET, and multilateral in EZ.

Author Contributions: Investigation, B.W. and C.G.; methodology, L.X. and C.G.; data curation, J.J. and Z.W.; writing—original draft preparation, B.W.; writing—review and editing, B.W. and Z.L.; supervision, C.G. and Y.B.; funding acquisition, C.G. and Y.B. All authors have read and agreed to the published version of the manuscript.

Funding: This work was supported by the National Natural Science Foundation of China (No. 52174297), Guangdong Basic and Applied Basic Research Foundation (No. 2022A1515110062), and Young Elite Scientists Sponsorship Program by CAST (No. 2022QNRC001).

Data Availability Statement: Data are contained within the article.

Conflicts of Interest: Author Jinwen Jin and Ze Wei were employed by the company Ningbo Iron and Steel Co., Ltd. The remaining authors declare that the research was conducted in the absence of any commercial or financial relationships that could be construed as a potential conflict of interest.

References

1. Li, X.; Li, B.; Liu, Z.; Niu, R.; Liu, Q.; Huang, X.; Xu, G.; Ruan, X. Detection and Numerical Simulation of Non-Metallic Inclusions in Continuous Casting Slab. *Steel Res. Int.* **2019**, *90*, 1800423. [[CrossRef](#)]
2. Chen, W.; Zhang, L.; Wang, Y.; Ren, Y.; Ren, Q.; Yang, W. Prediction on the three-dimensional spatial distribution of the number density of inclusions on the entire cross section of a steel continuous casting slab. *Int. J. Heat Mass Transf.* **2022**, *190*, 122789. [[CrossRef](#)]
3. Deng, X.; Wang, Q.; Ji, C.; Li, H.; Shao, X.; Liu, B.; Zhu, G. Three-dimensional distributions of large-sized inclusions in the surface layer of IF steel slabs. *Metall. Mater. Trans. B* **2020**, *51*, 318–326. [[CrossRef](#)]
4. Zhong, H.G.; Chen, X.R.; Liu, Y.J.; Wei, Z.Q.; Yu, H.F.; Zhai, Q.J. Influences of superheat and cooling intensity on macrostructure and macrosegregation of duplex stainless steel studied by thermal simulation. *J. Iron Steel Res. Int.* **2021**, *28*, 1125–1132. [[CrossRef](#)]
5. Zhang, P.; Xu, L.; Shi, P.; Yang, F.; Wang, M. Numerical and experimental investigation of solidification structure and macrosegregation in continuously cast 2311 die steel slab. *JOM* **2023**, *75*, 2853–2864. [[CrossRef](#)]
6. Koskenniska, S.; Kaijalainen, A.; Pikkarainen, T.; Mehtonen, S.; Porter, D.; Kömi, J. Effect of as-cast structure and macrosegregation on mechanical properties in direct-quenched low-alloy ultrahigh-strength steel. *Metall. Mater. Trans. B* **2021**, *52*, 95–106. [[CrossRef](#)]
7. Wang, C.; Liu, Z.; Li, B.; Dou, Z.; Rong, W. Effect of Alternate Electromagnetic Stirring on Macrostructure Evolution in Thin-Slab Continuous Casting. *Metall. Mater. Trans. B* **2024**, *55*, 2124–2137. [[CrossRef](#)]

8. Zhang, J.; Yan, L.; Xu, C.; Li, D.; Zhang, L. Effect of Slow Solidification of Ultra-thick Continuous Casting Slab on Solidification Structure and Macro-segregation. *Teh. Vjesn.* **2022**, *29*, 1171–1176.
9. Wu, Z.-H.; Mao, Q.-J.; Hua, F.-A.; Jia, G.-L.; Li, J.-P.; Li, C.-G.; Yuan, G.; Wang, G.-D. Researches on the Macro-and Micro-Structures and Properties of the Vertical Bending Continuous Casted AA6063 Thin Slabs and Their As-Rolled Sheets. *Metals* **2022**, *12*, 1937. [[CrossRef](#)]
10. Shabalov, I.; Matrosov, Y.; Kholodnyi, A.; Matrosov, M.; Velikodnev, V. Central Chemical and Structural Segregation Heterogeneity in Continuously Cast Slabs. *Pipeline Steels Sour Serv.* **2019**, *43*, 65–95.
11. Liang, J.; Song, C.; Wang, L.; Li, Z.; Zhai, Q. Study on macrostructure refinement of 12 wt-% Cr ferritic stainless steel slabs by TiN nucleation. *Mater. Technol.* **2012**, *27*, 333–336. [[CrossRef](#)]
12. Lekakh, S.N.; O'malley, R.; Emmendorfer, M.; Hrebec, B. Control of columnar to equiaxed transition in solidification macrostructure of austenitic stainless steel castings. *ISIJ Int.* **2017**, *57*, 824–832. [[CrossRef](#)]
13. Gao, X.; Yang, S.; Li, J. Effects of micro-alloying elements and continuous casting parameters on reducing segregation in continuously cast slab. *Mater. Des.* **2016**, *110*, 284–295. [[CrossRef](#)]
14. Choudhary, S.; Ganguly, S.; Sengupta, A.; Sharma, V. Solidification morphology and segregation in continuously cast steel slab. *J. Mater. Process. Technol.* **2017**, *243*, 312–321. [[CrossRef](#)]
15. Ganguly, S.; Choudhary, S. Quantification of the solidification microstructure in continuously-cast high-carbon steel billets. *Metall. Mater. Trans. B* **2009**, *40*, 397–404. [[CrossRef](#)]
16. Liu, D.M.; Xue, Z.L.; Song, S.Q. Effect of Manganese on the Formation Mechanism of Nonmetallic Inclusions in Fe-xMn-7Al-0.7C Lightweight Steel. *Steel Res. Int.* **2023**, *94*, 2200551. [[CrossRef](#)]
17. Que, G.R.; Song, S.Q.; Nyembwe, A.; Xue, Z.L.; Qi, J.H.; Deng, Z.X. TiN inclusions distribution in the composite cross section of Titanium Micro-alloyed Steel slab: Thermo-chemical modeling and automatic statistic analysis. *J. Mater. Res. Technol.* **2023**, *26*, 5383–5392. [[CrossRef](#)]
18. Li, X.A.; Wang, N.; Chen, M.; Du, Z.Q. Effect of Molten Steel Composition on Inclusion Modification by Calcium Treatment in Al-Killed Tinplate Steel. *ISIJ Int.* **2023**, *63*, 303–312. [[CrossRef](#)]
19. Zhao, S.; Li, Z.S.; Xu, R.Z.; Khasraw, D.; Song, G.Y.; Xu, D. Dissolution Behavior of Different Inclusions in High Al Steel Reacted with Refining Slags. *Metals* **2021**, *11*, 1801. [[CrossRef](#)]
20. Ren, Q.; Zhang, Y.; Ren, Y.; Zhang, L.; Wang, J.; Wang, Y. Prediction of spatial distribution of the composition of inclusions on the entire cross section of a linepipe steel continuous casting slab. *J. Mater. Sci. Technol.* **2021**, *61*, 147–158. [[CrossRef](#)]
21. Zhang, Q.; Yang, J.; Li, T.; Gong, J.; Huang, F.; Zhu, K.; Liu, F.; Liu, Z. Characteristics of Inclusions and Microstructures Around Solidification Hook of Low-Carbon Steel Continuous Casting Slab. *Metall. Mater. Trans. B* **2023**, *54*, 2439–2453. [[CrossRef](#)]
22. Chen, X.; Cheng, G.; Guo, J.; Pan, J. Transformation of inclusions in S32101 duplex stainless steel during continuous casting. *Metall. Res. Technol.* **2024**, *121*, 202. [[CrossRef](#)]
23. Wu, L.P.; Zhi, J.G.; Zhang, J.S.; Zhao, B.; Liu, Q. Effect of Cerium on the Microstructure and Inclusion Evolution of C-Mn Cryogenic Vessel Steels. *Materials* **2021**, *14*, 5262. [[CrossRef](#)] [[PubMed](#)]
24. Deng, X.; Ji, C.; Dong, W.; Li, L.; Yin, X.; Yang, Y.; McLean, A. Distribution of macro-inclusions in low carbon aluminium-killed steel slabs. *Ironmak. Steelmak.* **2018**, *45*, 592–602. [[CrossRef](#)]
25. Yu, Q.; Yang, X.; Lai, C.; Tong, Z. Study on mns inclusion aggregation along continuous casting slab thickness of medium carbon structural steel. *Metals* **2021**, *12*, 56. [[CrossRef](#)]
26. Ghosh, A.; Modak, P.; Dutta, R.; Chakrabarti, D. Effect of MnS inclusion and crystallographic texture on anisotropy in Charpy impact toughness of low carbon ferritic steel. *Mater. Sci. Eng. A* **2016**, *654*, 298–308. [[CrossRef](#)]
27. Wang, C.; Liu, X.-G.; Gui, J.-T.; Du, Z.-L.; Xu, Z.-F.; Guo, B.-F. Effect of MnS inclusions on plastic deformation and fracture behavior of the steel matrix at high temperature. *Vacuum* **2020**, *174*, 109209. [[CrossRef](#)]
28. Wu, M.; Fang, W.; Chen, R.-M.; Jiang, B.; Wang, H.-B.; Liu, Y.-Z.; Liang, H.-L. Mechanical anisotropy and local ductility in transverse tensile deformation in hot rolled steels: The role of MnS inclusions. *Mater. Sci. Eng. A* **2019**, *744*, 324–334. [[CrossRef](#)]
29. Yamamoto, K.-I.; Yamamura, H.; Suwa, Y. Behavior of non-metallic inclusions in steel during hot deformation and the effects of deformed inclusions on local ductility. *ISIJ Int.* **2011**, *51*, 1987–1994. [[CrossRef](#)]
30. Chu, J.; Nian, Y.; Zhang, L.; Bao, Y.; Ali, N.; Zhang, C.; Zhou, H. Formation, evolution and remove behavior of manganese-containing inclusions in medium/high manganese steels. *J. Mater. Res. Technol.* **2023**, *22*, 1505–1521. [[CrossRef](#)]
31. Kong, H.; Li, J.; Zhang, Z. Failure analysis of Q235B steel welded pipe. *Heat Treat. Met.* **2012**, *37*, 126–128.
32. Fan, W.; Sun, W.; Wang, H.; Ge, J.; Sun, B. Fracturing failure analysis of Q235B steel tube. *Heat Treat. Met.* **2010**, *35*, 75–77.
33. Zhao, G.; Huang, Q.; Zhang, Z.; Zhou, C.; Ma, L. Research on Microstructure and Mechanical Properties of Rolling Cladding Q235B Extra Thick Steel Plate. *Hot Work. Technol.* **2016**, *45*, 1–4.
34. Yao, C.; Wang, M.; Ni, Y.; Gong, J.; Gong, T.; Xing, L.; Bao, Y. Revealing the evolution mechanism from spot segregation to banded defect above the austenitization temperature. *J. Mater. Res. Technol.* **2023**, *26*, 6984–6993. [[CrossRef](#)]
35. Won, Y.-M.; Thomas, B.G. Simple model of microsegregation during solidification of steels. *Metall. Mater. Trans. A* **2001**, *32*, 1755–1767. [[CrossRef](#)]
36. Gu, C.; Bao, Y.P.; Lin, L. Cleanliness distribution of high-carbon chromium bearing steel billets and growth behavior of inclusions during solidification. *Rev. Metal.* **2017**, *53*, e089.

37. Xuechong, R.E.N.; Wuyang, C.H.U.; Jinxue, L.I.; Lijie, Q.; Yanjing, S.U. Effect of MnS inclusions on hydrogen diffusion in steel. *J. Univ. Sci. Technol. Beijing* **2007**, *29*, 232–236.
38. Wang, B.; Xing, L.; Li, X.; Bao, Y.; Wang, M. Study on Inclusions Distribution Across the Thickness of Enameled Steel Slabs. *Metall. Mater. Trans. B* **2024**, *55*, 4432–4445. [[CrossRef](#)]
39. Wang, Y.N.; Yang, J.; Wang, R.Z.; Xin, X.L.; Xu, L.Y. Effects of non-metallic inclusions on hot ductility of high manganese TWIP steels containing different aluminum contents. *Metall. Mater. Trans. B* **2016**, *47*, 1697–1712. [[CrossRef](#)]

Disclaimer/Publisher’s Note: The statements, opinions and data contained in all publications are solely those of the individual author(s) and contributor(s) and not of MDPI and/or the editor(s). MDPI and/or the editor(s) disclaim responsibility for any injury to people or property resulting from any ideas, methods, instructions or products referred to in the content.